Onset of sidebranching in directional solidification

Blas Echebarria
Departament de Física Aplicada, Universitat Politècnica de Catalunya, Av. Dr. Marañón 44-50, 08028 Barcelona, Spain

Alain Karma and Sebastian Gurevich
Department of Physics and Center for Interdisciplinary Research on Complex Systems, Northeastern University, Boston, Massachusetts 02115, USA

(Received 23 December 2009; published 26 February 2010)

We use a computationally efficient phase-field formulation [B. Echebarria *et al.*, Phys. Rev. E **70**, 061604 (2004)] to investigate the origin and dynamics of sidebranching in directional solidification for realistic parameters of a dilute alloy previously studied experimentally [M. Gorgelin and A. Pocheau, Phys. Rev. E **57**, 3189 (1998)]. Sidebranching is found to result either from noise amplification or from deterministic oscillations that exist both in two dimensions and in a three-dimensional thin-sample geometry. The oscillatory branch of growth solutions bifurcates subcritically from the main steady-state branch of solutions and exists over a finite range of large array spacings. In contrast, noise-induced sidebranching is associated with a smooth transition where the sidebranching amplitude increases exponentially with spacing up to nonlinear saturation due to the overlap of diffusion fields from neighboring cells, as observed experimentally. In the latter case where sidebranching is noise-induced, we find that increasing the externally imposed thermal gradient reduces the onset velocity and wavelength of sidebranching, as also observed experimentally. We show that this counterintuitive effect is due to tip blunting with increasing thermal gradient that promotes noise amplification in the tip region.

DOI: 10.1103/PhysRevE.81.021608 PACS number(s): 81.10.Aj, 64.70.dm, 81.30.Fb, 05.70.Ln

I. INTRODUCTION

Dendritic growth is a remarkable example of spontaneous pattern formation in nature of both fundamental and technological interest [1]. An ubiquitous feature of this growth process is the emission of secondary branches on the sides of a growing primary needlelike structure, and the subsequent emission of higher order branches leading to a highly organized treelike pattern [2–4]. For freely growing dendrites, where primary branches emerge from a solid seed along equivalent crystallographic directions, current theories attribute sidebranching to noise amplification [5–8]. Consistent with this prediction, phase-field simulations in two dimensions have shown that sidebranching without noise is only transient, and that the addition of noise produces the type of sidebranching activity observed experimentally [9]. At a more quantitative level, noise amplification theories predict that noise of microscopic origin should suffice to produce sidebranches when the departure of the needle crystal shape from a paraboloid of revolution far behind the tip is taken into account [3,8].

For cellular-dendritic arrays that form during the constrained solidification of an alloy in a thermal gradient, the origin of sidebranching has remained more poorly understood. In a casting, columnar dendrites are the predominant structures that grow with one preferred crystallographic axis generally aligned with the thermal gradient. Hence, they typically grow as an array of dendrites perpendicular to the cooler walls of the mold toward the hotter central liquid region of the casting. These structures can be studied in a more controlled way by directional solidification, i.e., by pulling a thin sample containing a binary alloy at constant velocity, V, parallel to the axis of an externally imposed temperature gradient, G [10]. The solid-liquid interface undergoes the classic Mullins-Sekerka instability when V exceeds a threshold value, V_c [11]. For V up to a few times V_c, the interface evolves after a long dynamical transient into a steady-state cellular array structure of wavelength (primary spacing) Λ, where cells are separated by narrow liquid grooves that become deeper with increasing V. For even higher velocities, cellular arrays become dendritic.

The transition from cell to dendrite is generally associated with a qualitative change in the cell tip shape, which becomes more parabolic with increasing growth rate. This shape change, in turn, promotes the appearance of sidebranches. The origin of the cell to dendrite transition has been studied experimentally for over two decades. In some experiments, this transition has been found to be accompanied by a discontinuous increase in primary spacing when cellular arrays become dendritic [12–14]. Numerical studies [15,16] have related this jump of spacing to the existence of different steady-state growth shapes for different spacings. Those studies showed that, for a range of intermediate growth velocities, cells and dendrites belong to different branches of solutions that exist only for small and large spacings, respectively, but not for spacings in between. In other experiments, however, the cell-to-dendrite transition has been observed to be continuous [17–20]. In those experiments, deep cells with blunt tips became progressively more needlelike and developed sidebranches of progressively larger amplitude as the primary spacing was increased at fixed velocity.

In this paper, we focus on understanding the formation of sidebranches in this latter case where the cell-to-dendrite transition is continuous as a function of the primary spacing Λ. This case is common experimentally since cells and dendrites generally belong to the same branch of steady-state growth solutions for large enough growth velocity. This was

highlighted in a recent phase-field study of steady-state growth shapes in two and three dimensions, which showed that, when the growth rate exceeds some threshold, the tip shape changes continuously from a blunt finger to a sharp needle with increasing Λ [16]. This threshold was also shown to depend sensitively on the magnitude of the surface energy anisotropy. As a basis of quantitative comparison for our predictions, we use the experiments of Refs. [17–20]. Those experiments exploited the history dependence of wavelength selection in directional solidification to select the array spacing and to maintain it spatially uniform [17], thereby making it possible to treat Λ as a control parameter on equal footing with G and V. Thus, those experiments explored the onset of sidebranching systematically in the three-dimensional (3D) parameter space (V,G,Λ) for a range of V where cells and dendrites belong to the same branch of steady-state growth solutions.

The experimental observations revealed that this space splits into two distinct domains of branched and nonbranched cells separated by a critical surface $V_{SB}(\Lambda,G)$, which defines the onset of sidebranching [17]. This onset turns out to be well-defined because the velocity range over which sidebranches become 'visible' is extremely narrow. The critical speed $V_{SB}(\Lambda,G)$ is a monotonously decreasing function of Λ at fixed G, consistent with the expectation that sidebranching can be induced by increasing either velocity or spacing. More surprising, however, was the finding that sidebranching is induced when G is increased at fixed V and Λ (i.e., $V_{SB}(\Lambda,G_2)<V_{SB}(\Lambda,G_1)$ if $G_2>G_1$). Naively, this observation appears counterintuitive since increasing G has a strong stabilizing effect on the primary instability.

So far, it has not been possible to extend the theory of noise amplification to directional solidification in order to explain those observations. While the tip shape in free growth is close to the Ivantsov paraboloid [21], the steady-state growth shape in directional solidification is not known analytically, except in two limiting cases. The first is the limit $\Lambda \ll l_D$, where the array spacing is much smaller than the solutal diffusion length $l_D \sim D/V$ where D is the solute diffusivity. In this limit, cells tip shapes are predicted to be well described by Saffman-Taylor fingers, based on the mathematical analogy between directional solidification in this limit and viscous fingering [33]. The second is the opposite limit $\Lambda \gg l_D$ where needle tips interact weakly via the diffusion field and grow essentially as free dendrites. For typical experimental spacings in between those two limits, approximate expressions for growth shapes have being obtained by matching the cell tip and tail regions [22]. Analytical expressions for cell shapes have also been derived empirically from fits to experimental observations [19]. However, the lack of reliable analytical solutions for steady-state shapes have hindered the extension of noise amplification theories to this problem.

The alternate possibility that sidebranching results from deterministic oscillations of the tip region was proposed previously for freely growing dendrites [23]. However, free-growth dendrites were subsequently shown numerically to be linearly stable [24] in support of a noise amplification mechanism. For directional solidification, a limit cycle behavior cannot be ruled out since the temperature gradient, absent in free growth, strongly influences the interface dynamics in the tip region. Recent experimental analysis of the bursting behavior of sidebranches in fact suggests the existence of a nonlinear limit cycle [25].

In this paper, we use phase-field simulations to shed light on the origin of sidebranching in directional solidification. Our main goal is to sort out to what degree the sidebranching activity is due to noise or deterministic dynamics. A secondary goal is to explain the counterintuitive experimental observation that increasing the magnitude of the thermal gradient promotes sidebranching. As in the experiments where this observation was made [17], we treat the cell spacing Λ as a control parameter together with V and G. We do not address here the question of how Λ is dynamically selected, which is not essential for understanding the nature of the critical surface separating branched and nonbranched structures. We use a quantitative phase-field formulation for the directional solidification of dilute binary alloys in the experimentally relevant low velocity limit of local equilibrium at the interface [26,27]. In addition, we exploit the fact that a phase-field approach is ideally suited to study quantitatively the effect of a small amplitude thermal noise [9].

Our main finding is that sidebranching can be due either to noise amplification or to a nonlinear limit cycle. When increasing the array spacing in the presence of noise, we find that sidebranches increase exponentially in amplitude above some critical spacing that depends both on growth rate and temperature gradient. Furthermore, in a large spacing range where sidebranches already form due to noise amplification, a limit cycle bifurcates subcritically with increasing Λ from the underlying branch of steady-state cells. Sustained oscillations appear due to a resonant interaction in which sidebranches produce a perturbation of the tip, which in turn becomes amplified, creating a positive feedback. While recent experiments have hinted to the existence of a limit cycle [25], we are able to demonstrate unequivocally its existence by showing that tip oscillations persists over a finite range of spacings in simulations in which noise is switched off. When noise is switched back on, this oscillatory state is found to coexist with a state with noise-induced sidebranches of smaller amplitude. This limit cycle, therefore, provides a natural explanation for bursts of almost periodic sidebranches that have been recently evidenced experimentally [20,25].

In addition, our results shed light on the role of the thermal gradient. We find that increasing G makes the cell tip shape more blunt and hence more susceptible to noise, thereby promoting sidebranching. The results also provides detailed quantitative insights into the characteristics of sidebranching, including the dependence of the sidebranch amplitude and spacing on the distance behind the tip and the control parameters. Due to the amount of computational time needed to investigate the (V,G,Λ) parameter space, we perform primarily two-dimensional (2D) simulations. However, we also present three-dimensional simulations that confirm the existence of a limit cycle in three dimensions.

The paper is organized as follows. In Sec. II, we write down sharp-interface equations that describe the directional solidification of a dilute binary alloy with the incorporation of thermodynamic fluctuations. The corresponding phase-

field equations that reduce to those equations in a computationally tractable thin-interface limit are then discussed in Sec. III. Next, we present and discuss in Sec. IV the results of the phase-field simulations. Finally, concluding remarks and future prospects are given in Sec. V. The application of noise amplification theories to directional solidification are discussed in the Appendix.

II. SHARP-INTERFACE MODEL

We model the directional solidification of a dilute binary alloy with solvent A and solute B atoms. In the dilute limit, the liquidus and solidus are straight lines of slopes m and m/k, respectively, where k is the partition coefficient. The interface is assumed to be in local equilibrium with a local growth temperature given by the Gibbs-Thomson relation

$$T = T_m - |m|c_l - \Gamma\mathcal{K}, \tag{1}$$

and the concentrations on the solid (c_s) and liquid (c_l) sides of the interface (defined as mole fractions of the dilute impurity B) related by

$$c_s = kc_l, \tag{2}$$

where T_m is the melting temperature of pure A, $\Gamma=\gamma T_m/L$ is the Gibbs-Thomson coefficient, γ is the surface energy, L is the latent heat of fusion per unit volume, $\mathcal{K}$ is the local interface curvature, and V_n is the interface normal velocity. Surface tension is assumed isotropic for simplicity here, but anisotropy is incorporated in the phase-field model.

We use the frozen temperature approximation

$$T(z) = T_0 + G(z - V_p t), \tag{3}$$

which assumes that the rejection of latent heat has a negligible effect. Furthermore, we use the so-called "one-sided" approximation that assumes zero solute diffusivity in the solid. The concentration field then obeys the set of equations

$$\partial_t c = D\nabla^2 c - \vec{\nabla}\cdot\vec{j}_c, \tag{4}$$

$$c_l(1-k)V_n = -D\partial_n c|^+ + \hat{n}\cdot\vec{j}_c, \tag{5}$$

$$c_l/c_l^0 = 1 - (1-k)d_0\mathcal{K} - (1-k)\beta V_n - (1-k)(z - V_p t)/l_T, \tag{6}$$

where $\partial_n c|^+$ is the normal gradient of concentration on the liquid side of the interface, $d_0=\Gamma/\Delta T_0$ is the chemical capillary length, $\Delta T_0=|m|(1-k)c_l^0$ is the freezing range, and $l_T=|m|(1-k)c_l^0/G$ is the thermal length. Equation (6) is obtained using Eqs. (1) and (3), where $c_l^0=(T_m-T_0)/|m|=c_\infty/k$, is the equilibrium concentration on the liquid side of a steady-state planar interface at T_0, and $c_\infty\equiv c(z=+\infty)$ is the alloy composition.

Concentration fluctuations in the liquid are represented by the current $\vec{j}_c=j_c^x\hat{x}+j_c^z\hat{z}$, whose components are random variables obeying a Gaussian distribution with variance

$$\langle j_c^m(\vec{r},t)j_c^n(\vec{r}',t')\rangle = 2DF_c\delta_{mn}\delta(\vec{r}-\vec{r}')\delta(t-t'). \tag{7}$$

The noise magnitude F_c is determined through the fluctuation-dissipation relation

$$\langle(\delta c)^2\rangle = \frac{c}{(N_A/v_0)\Delta V} = \frac{F_c}{\Delta V}, \tag{8}$$

where $\langle(\delta c)^2\rangle$ is the equilibrium average of the square of the departure of the concentration from its equilibrium value inside a microscopically large but macroscopically small volume ΔV. The first equality in Eq. (8) above follows straightforwardly from the standard relation $\langle(\delta n)^2\rangle=n$, where n is the number of solute atoms in the small volume ΔV. Using the definition $c=n/N$, and the expression $N=\Delta V N_A/v_0$ for the number of solvent atoms in the same volume, where N_A is Avogadro's number and v_0 is molar volume of solvent atoms, we obtain at once Eq. (8). The second equality on the right-hand side of Eq. (8) is obtained by computing $\langle(\delta c)^2\rangle$ directly from the sharp-interface Eqs. (4)–(7) and is a simple form of the fluctuation-dissipation theorem.

To facilitate the link between sharp- and diffuse-interface models, we rewrite Eqs. (4)–(7) in terms of the local supersaturation with respect to the point (c_l^0,T_0), measured in units of the equilibrium concentration gap at that point,

$$U = \frac{c - c_l^0}{\Delta c_0}, \tag{9}$$

where we have defined $\Delta c_0=c_l^0(1-k)=c_\infty(1/k-1)$, which corresponds to the concentration jump at a reference moving planar interface with concentration $c_l^0=c_\infty/k$ (c_∞) on the liquid (solid) side of the interface. We obtain

$$\partial_t U = D\nabla^2 U - \vec{\nabla}\cdot\vec{j}_u \quad \text{(liquid)}, \tag{10}$$

$$[1+(1-k)U]V_n = -D\partial_n U|^+ + \hat{n}\cdot\vec{j}_u \quad \text{(interface)}, \tag{11}$$

$$U = -d_0\mathcal{K} - \beta V_n - (z - V_p t)/l_T \quad \text{(interface)}, \tag{12}$$

with

$$\langle j_u^m(\vec{r},t)j_u^n(\vec{r}',t')\rangle = 2DF_u\delta_{mn}\delta(\vec{r}-\vec{r}')\delta(t-t'), \tag{13}$$

and F_u defined via the relation

$$\langle(\delta U)^2\rangle = \frac{\langle(\delta c)^2\rangle}{(\Delta c_0)^2} \equiv \frac{F_u}{\Delta V}. \tag{14}$$

Combining Eqs. (8) and (9) with the above second equality, we obtain that

$$F_u = F_u^0[1+(1-k)U], \tag{15}$$

where we have defined the constant noise magnitude

$$F_u^0 = \frac{kv_0}{(1-k)^2 N_A c_\infty}, \tag{16}$$

which is the value of F_u for the reference planar interface at temperature T_0 ($U=0$).

For completeness, it is instructive to show that the present incorporation of noise in the sharp-interface model yields the correct equilibrium interface fluctuation spectrum. Following the procedure outlined in Refs. [28], this spectrum can be calculated from Eqs. (10)–(13) by considering a planar inter-

face in the limit of vanishing growth rate, which is essentially in equilibrium with c_∞/k (c_∞) on the liquid (solid) side of the interface. The result is

$$\langle z_q z_{-q}\rangle = \frac{F_u}{d_0 q^2} = \frac{k_B T}{\gamma q^2}, \tag{17}$$

where z_q is the Fourier coefficient defined in two dimensions by $z(x)=(1/2\pi)\int dq\, \exp(iqx) z_q$ where $z(x)$ is the interface profile. The second equality above is obtained by eliminating F_u using (i) the expression for the chemical capillary length $d_0=\Gamma/[|m|c_\infty(1/k-1)]$, (ii) the definition of the Gibbs-Thomson coefficient $\Gamma=\gamma T_0/L$, where L is the latent heat of melting per unit volume and γ is the surface energy, and (iii) the Clausius-Clapeyron relation $|m|/(1-k)=k_B T_0^2/(L v_0/N_A)$ where $L v_0/N_A$ is the latent heat per mole.

III. PHASE-FIELD MODEL

A. Basic equations

We use a phase-field formulation of dilute-alloy directional solidification that makes use of an "antitrapping" current [26] to model the limit of local thermodynamic equilibrium at the solid-liquid interface. The equations of this model are described in details in Ref. [27]. They reduce to the sharp-interface model of the previous section in a computationally tractable thin-interface limit where the interface thickness is only constrained to be chosen smaller than the characteristic scale of the pattern (e.g., the cell tip radius), but can be much larger than the nanometer width of a real interface. The complete set of phase-field equations including crystalline anisotropy are given by

$$\begin{aligned}\tau_\phi(\hat{n},z)\frac{\partial\phi}{\partial t} &= \vec{\nabla}\cdot[W(\hat{n})^2\vec{\nabla}\phi] + \partial_x\left(|\vec{\nabla}\phi|^2 W(\hat{n})\frac{\partial W(\hat{n})}{\partial(\partial_x\phi)}\right)\\ &+ \partial_z\left(|\vec{\nabla}\phi|^2 W(\hat{n})\frac{\partial W(\hat{n})}{\partial(\partial_z\phi)}\right)\\ &+ \phi-\phi^3-\lambda g'(\phi)\left(U+\frac{z-V_p t}{l_T}\right),\end{aligned} \tag{18}$$

$$\tau_U\frac{\partial U}{\partial t} = \vec{\nabla}\cdot(Dq(\phi)\vec{\nabla}U+\vec{j}_{at}) + [1+(1-k)U]\frac{1}{2}\frac{\partial\phi}{\partial t} - \vec{\nabla}\cdot\vec{J}, \tag{19}$$

with

$$U=\frac{1}{1-k}\left[\frac{c/c_l^0}{(1-\phi)/2+k(1+\phi)/2}-1\right], \quad q(\phi)=(1-\phi)/2, \tag{20}$$

$$\vec{j}_{at} = (1/2\sqrt{2})W[1+(1-k)U]\frac{\partial\phi}{\partial t}\frac{\vec{\nabla}\phi}{|\vec{\nabla}\phi|}, \tag{21}$$

$$\tau_\phi(\hat{n},z)=\tau(\hat{n})[1-(1-k)(z-V_p t)/l_T],$$

$$\tau_U=[1+k-(1-k)\phi]/2. \tag{22}$$

The correlation of the fluctuating current

TABLE I. Parameters for the impure succinonitrile (SCN) alloy system of Ref. [17] used in the phase-field simulations and corresponding characteristic length scales for directional solidification. The anisotropy of the interfacial free energy is taken to be $\epsilon_4=0.007$ (0.7% anisotropy).

$\lvert m\rvert c_\infty$ (shift in melting temperature)	2 K
D (diffusion coefficient)	10^{-9} m^2/s
Γ (Gibbs-Thompson coefficient)	6.48×10^{-8} Km
V_p (pulling speed)	8–32 μm/s
G (thermal gradient)	35–140 K/cm
d_0 (capillary length)	1.3×10^{-2} μm
l_T (thermal length)	$3.33-13.33\times10^2$ μm
l_D (diffusion length)	62.5–250 μm
k (partition coefficient)	0.3

$$\langle J^m(\vec{r},t)J^n(\vec{r}',t')\rangle = 2Dq(\phi)F_u^0[1+(1-k)U] \times\delta_{mn}\delta(\vec{r}-\vec{r}')\delta(t-t'), \tag{23}$$

now depends explicitly on the phase-field ϕ via the solute diffusivity $Dq(\phi)$ that vanishes in the solid and has a constant value D in the liquid. Equation (23) reduces to Eq. (13) of the sharp-interface model in the liquid phase and F_u^0 is defined as before by Eq. (16). The orientation-dependent functions $W(\hat{n})$ and $\tau(\hat{n})$ are related by $W(\hat{n})=Wa_s(\hat{n})$ and $\tau(\hat{n})=\tau_0(a_s(\hat{n}))^2$ [27,29], where $\hat{n}=-\vec{\nabla}\phi/|\vec{\nabla}\phi|$ is the normal to the interface, and we choose here a fourfold crystalline anisotropy $a_s(\hat{n})=1-3\epsilon_4+4\epsilon_4(n_x^4+n_z^4)$, which yields

$$a_s(\hat{n}) = 1-3\epsilon_4+4\epsilon_4\sum_{m=x,z}\partial_m^4\phi/|\vec{\nabla}\phi|^4. \tag{24}$$

Finally, the above equations are easily extended to three dimensions by adding partial derivative terms in y that are identical to those in x.

B. Computational parameters

We have simulated the phase-field model of the directional solidification of a dilute binary alloy defined by the anisotropic version of Eqs. (18) and (19) for parameters corresponding to the impure succinonitrile (SCN) alloy of Ref. [17]. The alloy parameters together with the range of values of the pulling speed and the temperature gradient are listed in Table I. To choose the phase-field model parameters, we first note that the ratio of the capillary and thermal lengths, $\nu=d_0/l_T$, and the dimensionless pulling speed $v_p=V_p d_0/D$ completely specify the interface evolution in the sharp-interface equations. This can be seen by scaling length and time in these equations by d_0 and d_0^2/D, respectively. In the phase-field model, we have the additional length W and converged results should be independent of the ratio $\epsilon=W/d_0$. The coupling constant is then obtained from $\lambda=a_1 W/d_0=a_1\epsilon$ [27]. In order to avoid kinetic effects, absent for solidification at low pulling speeds, we have to impose the additional constraint: $D=a_2\lambda W^2/\tau_0=a_1 a_2\epsilon W^2/\tau_0$ [27]. We have chosen the phase-field parameters in such a way that the pulling speed is constant in phase-field units

TABLE II. Parameters in the phase-field equations.

	$\epsilon = W/d_0$	$D\tau_0/W^2$	λ
$V_p = 32\ \mu$m/s	36.1	20	31.91
$V_p = 20.5\ \mu$m/s	45.1	25	39.89
$V_p = 8\ \mu$m/s	72.2	40	63.82

$V_p\tau_0/W = 0.3$. This implies, using the former expressions, that the value of ϵ must be $\epsilon = (0.3D/a_1a_2V_pd_0)^{1/2} = (0.3/a_1a_2v_p)^{1/2}$, which completely specifies the problem. The resulting values of the parameters in the phase-field Eqs. (18) and (19) are shown in Table II. For the present values of $\epsilon = 36-72$, the system has been shown to be fairly well resolved [27]. Still, one could expect a discrepancy of about a 10% in the tip radius for the lower pulling speed (larger ϵ), resulting in a flatter tip.

Equations (18) and (19) are discretized with finite difference formulas and time stepped with a simple Euler scheme. For the Laplacian of the phase field, we use the maximally isotropic discretization,

$$(\Delta x)^2\nabla^2\phi_{i,j} = \frac{2}{3}\Big[\phi_{i+1,j} + \phi_{i-1,j} + \phi_{i,j+1} + \phi_{i,j-1} + \frac{1}{4}(\phi_{i+1,j+1} + \phi_{i-1,j+1} + \phi_{i+1,j-1} + \phi_{i-1,j-1}) - 5\phi_{i,j}\Big], \quad (25)$$

which avoids the grid corrections to the anisotropy that are discussed in Ref. [29]. For the anisotropy of SCN we take the value $\epsilon_4 = 0.7\%$.

As in Ref. [9], the noise was discretized in the form

$$\vec{\nabla}\cdot\vec{J} \approx (J^k_{x,i+1j} - J^k_{x,ij} + J^k_{z,ij+1} - J^k_{z,ij})/\Delta x \quad (26)$$

where $J^k_{x,ij}$ and $J^k_{z,ij}$ are independent Gaussian random numbers with variance

$$\langle J^k_{m,ij}J^l_{m,i'j'}\rangle = 2Dq(\phi)[1 + (1-k)U]\frac{F^0_u}{\Delta x^2\Delta t}\delta_{ii'}\delta_{jj'}\delta_{kl}, \quad (27)$$

where the superscripts k and l refer to discrete times $t = k\Delta t$ and $t' = l\Delta t$. The above algorithm conserves U as long as nonflux boundary conditions are applied to the random variables $J^k_{m,ij}$. It follows from Eq. (27) above that the magnitude of noise is generally proportional to $F^0_u/\Delta x^d$ in d dimensions. Since Δx is proportional to the interface thickness, i.e., $\Delta x/W$ is set to a fixed value in the range 0.4 to 0.8 for numerical accuracy, $F^0_u/\Delta x^d$ increases when the interface thickness is decreased in the computations to examine the convergence of the results. Therefore, unless otherwise stated, we choose in our two-dimensional simulations $F^0_u = \bar{F}^0_u/\lambda^2$, with $\bar{F}^0_u = 10^{-7}$, where the factor of λ accounts for the variation in the effective noise amplitude with interface thickness.

IV. NUMERICAL RESULTS

The parameters in the phase-field model were chosen to reproduce the experimental situation in [17]. The characteristics and evolution of the cells were studied as a function of velocity and wavelength for different temperature gradients G ($G = 35, 70, 105, 140$ K/cm, corresponding to $\nu = d_0/l_T = 1-4\cdot10^{-5}$) and of the pulling speeds ($V_p = 8, 20.5, 32\ \mu$m/s). It should be stressed that a complete quantitative agreement with experiments is difficult to reach, due to the uncertainty in some of the parameters, and also to

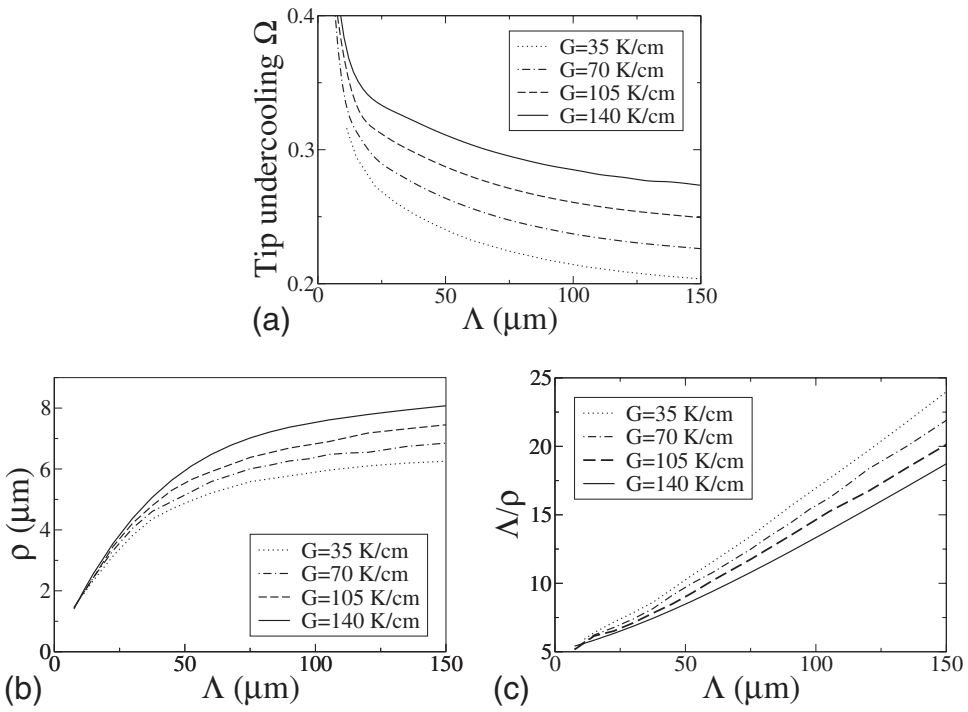

FIG. 1. Tip (a) undercooling Ω, (b) radius ρ, and (c) spacing over radius Λ/ρ, as a function of the cell spacing Λ, for fixed pulling speed $V_p = 32\ \mu$m/s $\simeq 10\ V_c$, and several values of the thermal gradient G.

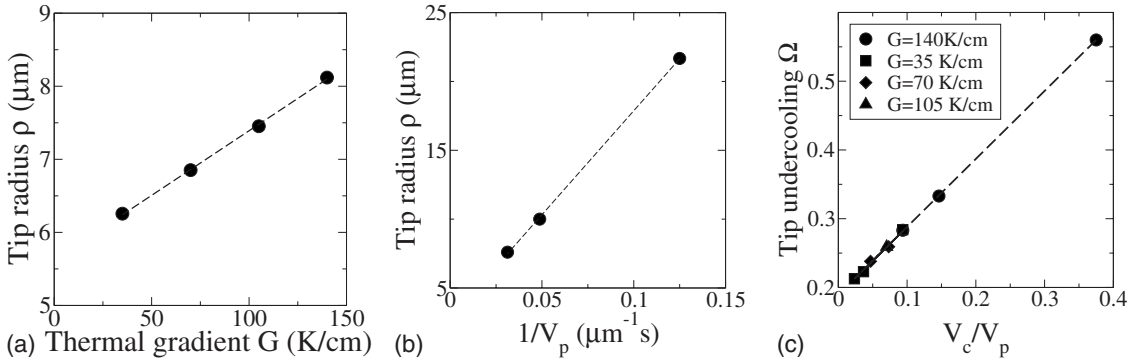

FIG. 2. (a) Tip radius as a function of thermal gradient for $V_p=32$ μm/s, $\Lambda=150$ μm/s. (b) Tip radius vs pulling speed for $G=140$ K/cm and $\Lambda=105$ μm. (c) Tip undercooling vs V_c/V_p for the same spacing and various temperature gradients.

the fact that our simulations are two-dimensional, while in experiments cells are fully three-dimensional. Any difference in the cell shape can affect the amplification of sidebranches, both at the tip, and along the sides. However, we expect our results to be valid qualitatively, and even to obtain a semiquantitative agreement with experimental results.

A. Characterization of the cells and their instabilities

For given G and V_p, we study the characteristics of the cells as a function of cell spacing Λ. For computational convenience, we simulate only half a cell $x \in [0, \Lambda/2]$, with nonflux boundary conditions on the sides. We start with a cell at a small cell spacing and then increase the spacing at intervals of $\Delta\Lambda \sim 7$ μm, after which the system is allowed to relax for about 50 diffusion times to its new state. The first cell is obtained starting from the equilibrium concentrations at $z=l_T$, adding a sinusoidal perturbation, and letting it relax to its final configuration as half a cell. In some cases we simulate one or two full cells. This was necessary to study, for instance, the cell elimination instability.

In Fig. 1, we show the tip radius ρ and dimensionless tip undercooling $\Omega=1-z_{\text{tip}}/l_T$ for the cellular branch, as a function of the cell spacing, obtained simulating Eqs. (18) and (19) *without* noise. This provides us with the deterministic branch onto which fluctuations will be later added. From these results it is clear that there is a single cellular branch, and we therefore expect a smooth transition to sidebranching. Depending on the ratio $\Lambda/l_D=\Lambda V_p/2D$ we can distinguish two different regimes: at small cell spacings ($\Lambda \ll l_D=62.5$ μm) the cells become self-similar, with a tip radius proportional to the width of the cell (similar to a Saffman-Taylor finger), while at cell spacings much larger that the diffusion length, the tip radius becomes constant, and the cells dendritelike. As we have already mentioned, the values of both ρ and Ω will change with respect to those obtained in full 3D simulations. In typical experiments, the depth of the sample is comparable to the cell spacing, and therefore the cells are fully three-dimensional. Comparisons of phase-field simulations of 2D and 3D cells have shown that the tip radius is systematically smaller in 2D, and the tip undercooling larger [16,30]. This agrees with experimental

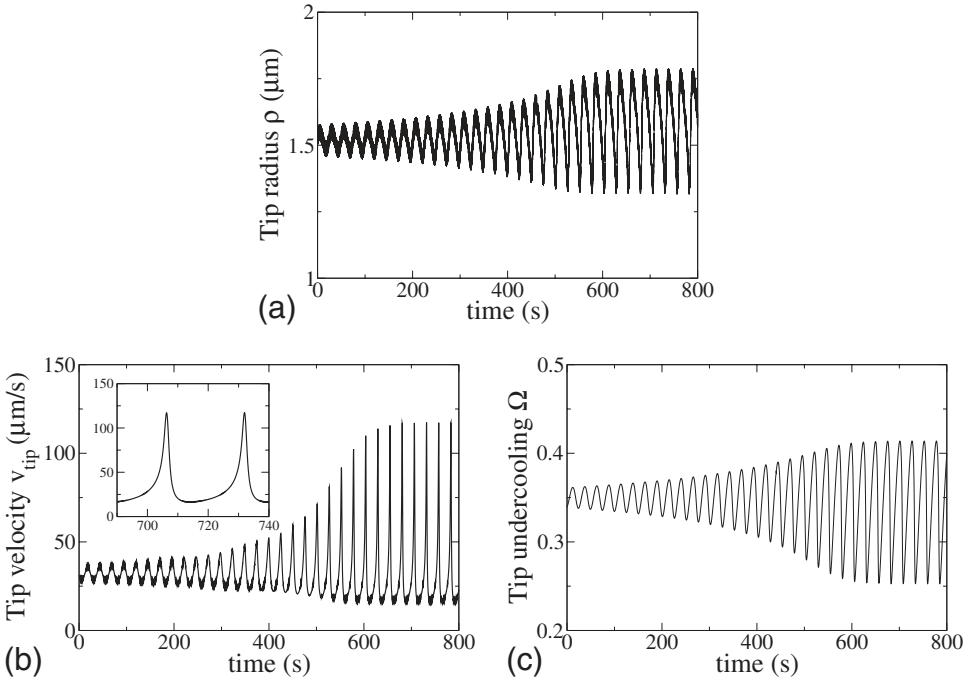

FIG. 3. Oscillations in (a) tip radius, (b) tip velocity, and (c) tip undercooling in a cell of $\Lambda=8.26$ μm, at $G=35$ K/cm and $V_p=32$ μm/s. As initial condition we take the final state of a simulation with $\Lambda=9.01$ μm, which does not present sustained oscillations.

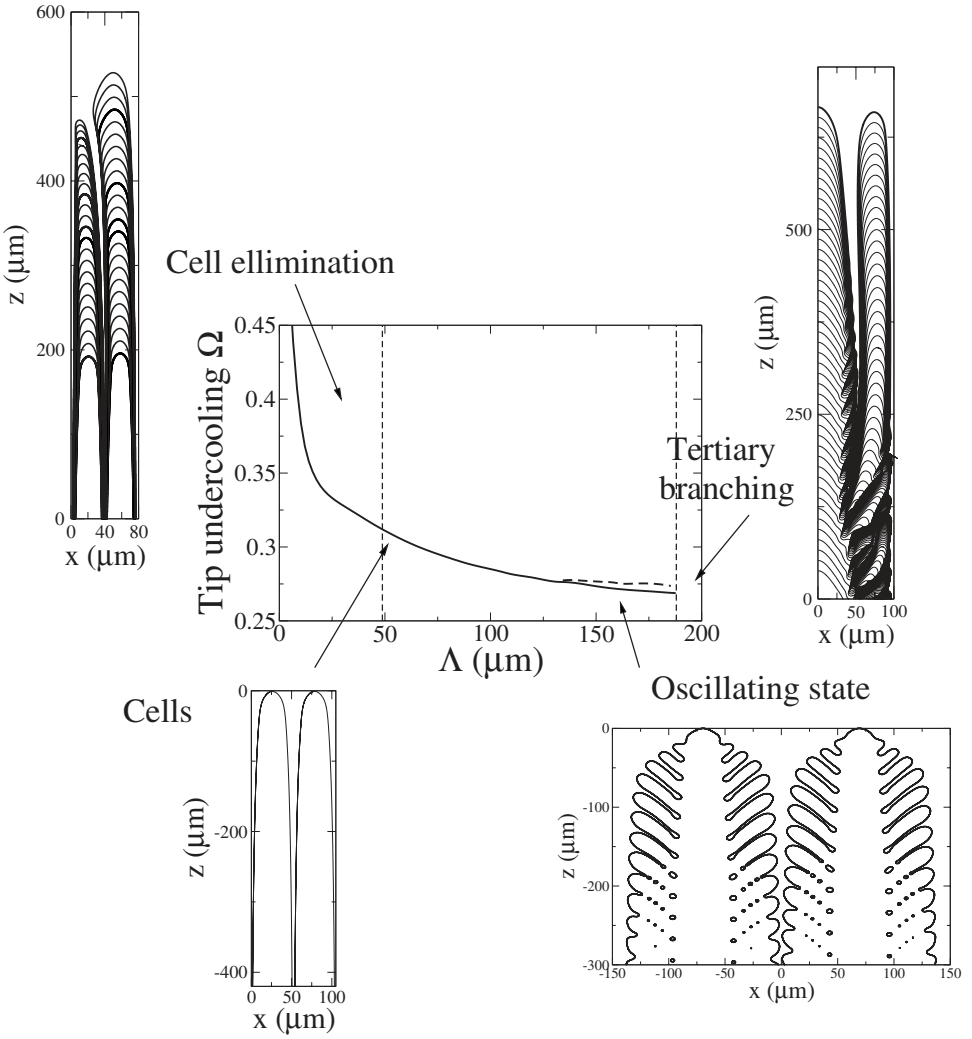

FIG. 4. Limits of stable cells, and their different instabilities, as a function of Λ, for $G=140$ K/cm, $V_p=32$ μm/s $\simeq 10$ V_c. The branch of oscillating state is bistable with sidebranches induced by noise.

measures of the tip radius, that is found to be larger than in our present simulations (i.e., $\rho \sim 16.5$ μm, in [31], for $\Lambda \simeq 105$ μm, $G=140$ K/cm, and $V_p=20$ μm/s vs $\rho \sim 10$ μm in our simulations). Alternatively, since the tip radius depends sensitively on the anisotropy, one cannot completely discard that our value of the anisotropy overestimates that in real experiments. In whichever case, a larger tip means that sidebranching will be expected to occur for a smaller value of cell spacing in experiments than in our simulations. For all these considerations, we do not expect a perfect quantitative agreement on the onset and characteristics of sidebranches. However, we expect to be able to obtain the right trends and even a semiquantitative agreement. For a complete quantitative agreement with experimental results, 3D simulations of solidification cells are needed.

In Figs. 2(a) and 2(b), we show the dependence of the tip radius on thermal gradient and pulling speed. In [31] the following relation was found: $\rho \propto V_p^{-1/4}\Lambda^{3/4}G^{1/2}$, that fitted the experimental results over a wide range of parameters. We find, however, that for fixed Λ and V_p the tip radius seems to be nearly proportional to the thermal gradient $\rho \propto G$ (Fig. 2(a)). The change with G is, therefore, larger in our simulations than in experiments, and we expect this to be also reflected in a stronger dependence of the onset of sidebranching with thermal gradient. As for the tip undercooling, in [32], they found that measurements at different temperature gradients all collapsed into the relation $\Omega=V_c/V$. From Fig. 2(c), we see that our results at different temperature gradients also collapse to a single line, with the fit $\Omega=0.189+0.989V_c/V_p$. Thus, the slope seems to agree well with [32], but with this fit the undercooling does not go to zero as $V_p \to \infty$. Again we presume that the main difference will be due to the two-dimensional nature of our cells, since 3D cells typically present a lower undercooling than their two-dimensional counterparts [16,30].

At small cell spacings we encounter the well known oscillatory instability of deep cells [33]. It results in big oscillations in the velocity and position of the tip (Fig. 3). Both the critical value of the cell spacing for the onset of the instability, and the frequency of oscillations agree perfectly with the theoretical predictions. For $k=0.3$ and $\nu=V_p l_T/2D=21.33$ (corresponding to $V_p=32$ μm/s and $G=35$ K/cm), the instability is predicted for a value of

$$\frac{k(1-1/2\nu)}{1-(1-k)\lambda}\frac{\Lambda^2 V_p}{d_0 D} \simeq 90, \tag{28}$$

where the relative cell width λ can be obtained fitting the tip region to a Saffman-Taylor finger, in which case we obtain $\lambda \simeq 0.58$. Then, the critical value of the cell spacing results

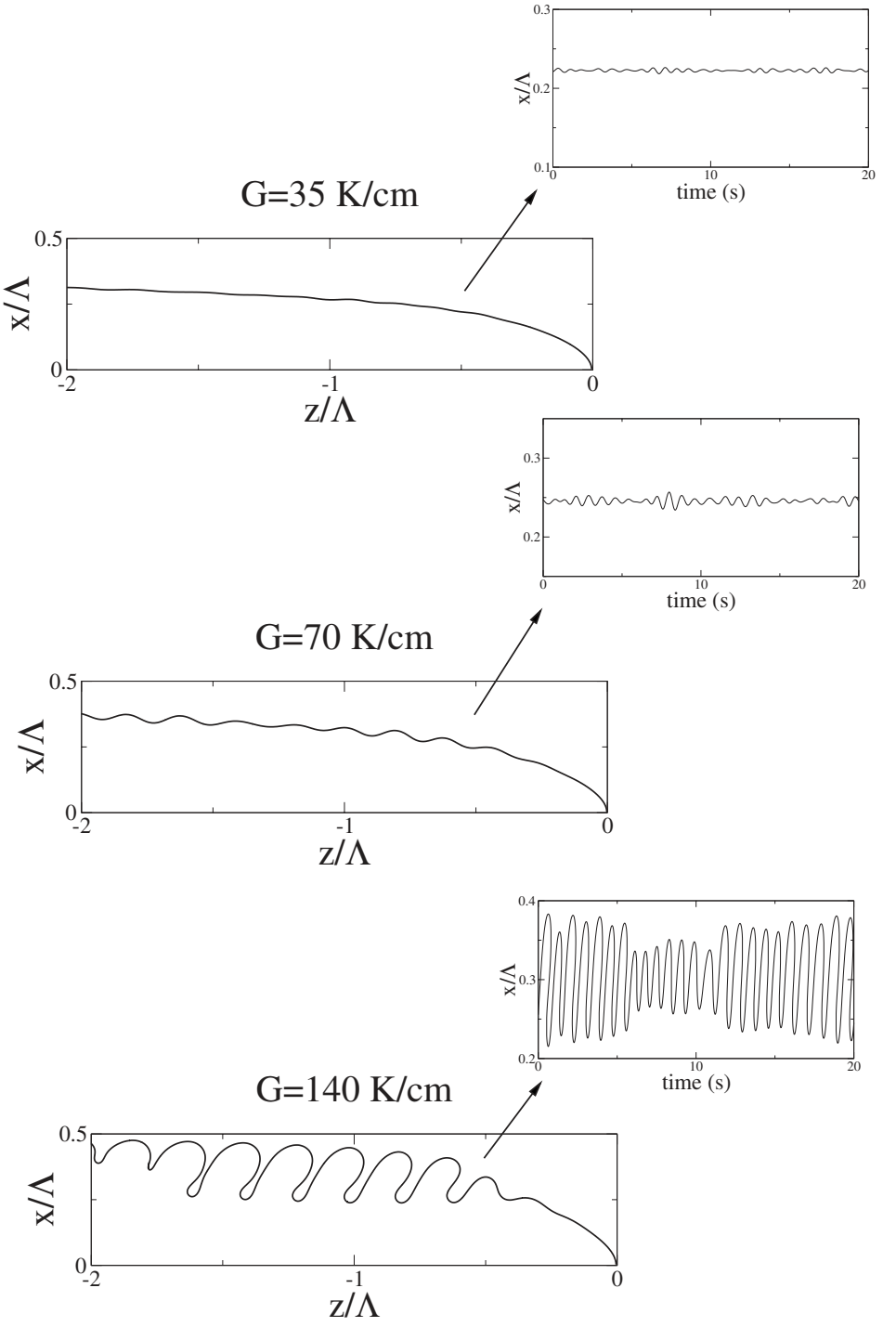

FIG. 5. Interfacial shapes for three different thermal gradients, and time series of the interface at a point 38 μm behind the tip, at fixed $\Lambda=105$ μm, and $V_p=32$ μm/s$\simeq 10$ V_c.

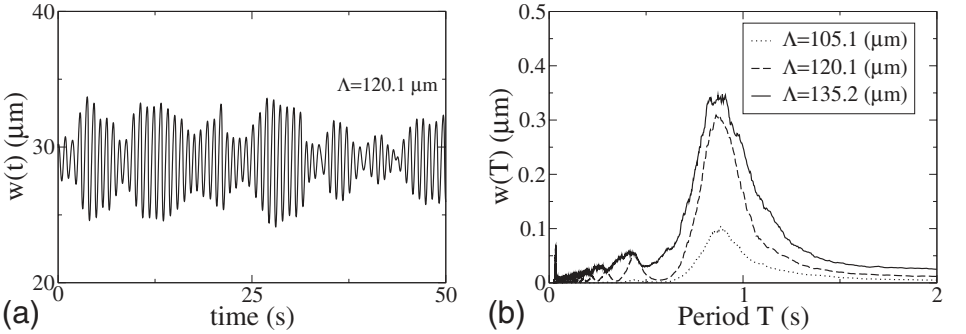

FIG. 6. (a) Time series of the position of the interface at a point 38 μm$\simeq 4.5\rho$ ($\rho=8$ μm) behind the tip, for $\Lambda=120.1$ μm, and (b) Fourier spectrum for several cell spacings (the final result has been smoothed). The rest of the parameters are $G=140$ K/cm, $V_p=32$ μm/s$\simeq 10$ V_c. The peak of the spectrum occurs at approximately $T\simeq 0.88$ s.

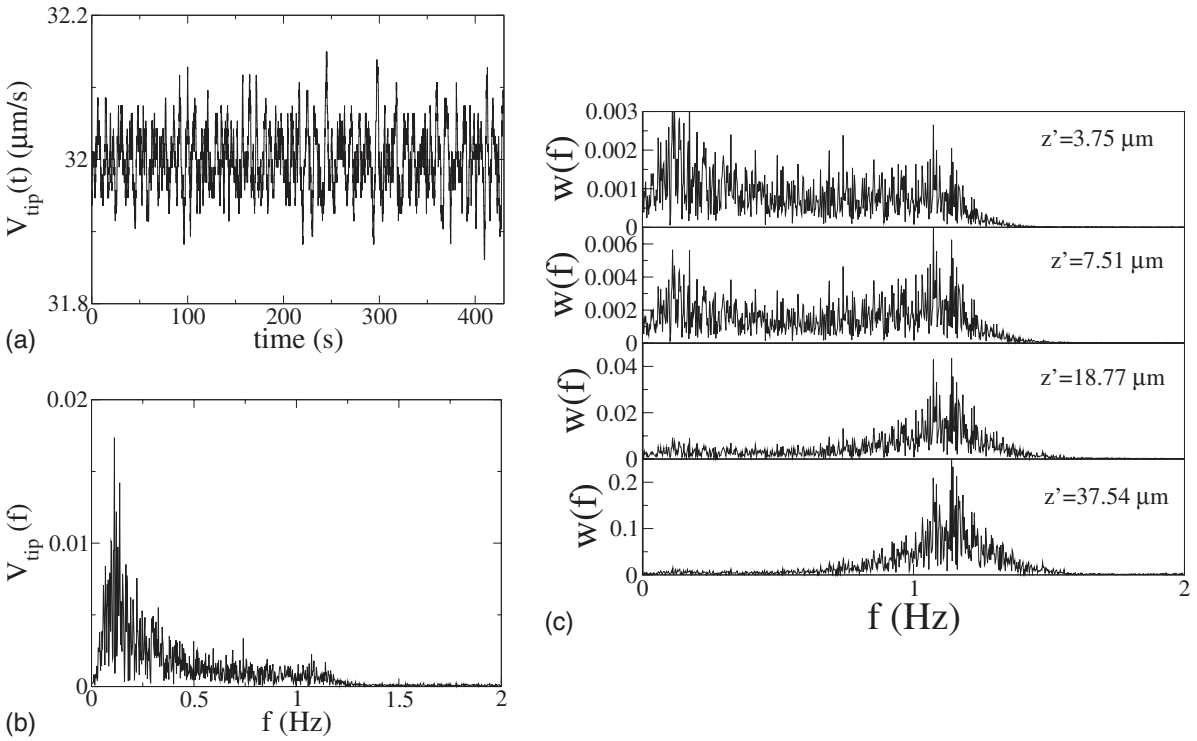

FIG. 7. (a) Tip velocity, (b) its Fourier spectrum, and (c) Fourier spectrum of the interface position at several distances behind the tip, for $\Lambda=105$ μm, $V_p=32$ μm/s, and $G=140$ K/cm.

$\Lambda_c=8.6$ μm, while in the numerical simulations the onset is located somewhere between $\Lambda=8.26$ μm and $\Lambda=9.01$ μm. For the frequency the prediction is $\omega=(1+k)V_p^2/(2D\sqrt{k\nu})=0.263$ rad/s (with the corresponding period $T=23.9$ s), to be compared with the numerical result of $\omega=0.25$ rad/s at $\Lambda=8.26$ μm.

In practice, this region of self-similar solutions is never reached in an array of cells (remember that up to this point all the results we have shown have been obtained with half a cell). For small values of Λ, there is a cell elimination instability (see Fig. 4) in which one out of two cells disappears, thus doubling the wavelength of the cellular array. For large cell spacings there is another instability limiting the region of stable cells, the tail instability, where a perturbation at the tail will grow into a new cell. If there is sidebranching activity prior to reaching this instability, then one of the sidebranches will be responsible of creating a new cell, resulting in tertiary branching. Sidebranching will occur at an intermediate value of the cell spacing, and therefore in a region where the cells are neither Saffman-Taylor-like, nor dendritelike. Thus the difficulty to treat the problem analytically.

The cell branch, however, is not the only possible solution. At large cell spacings there exists also a branch of cells with perfectly periodic sidebranches (Fig. 4). They appear through a subcritical Hopf bifurcation off the cell branch, and are bistable with cells for a range of cell spacings. Thus, these are not noise-induced sidebranches, but completely deterministic. We will defer a complete analysis of this branch until Sec. IV C, and study first the effect of noise on the cell branch.

B. Sidebranching

To study the onset of sidebranching we add noise to the cell states obtained in the previous section, and let the system evolve. Sidebranches are artificially constrained to grow symmetrically about the tip and to grow into a rigid side wall because of the reflective boundary conditions imposed on the

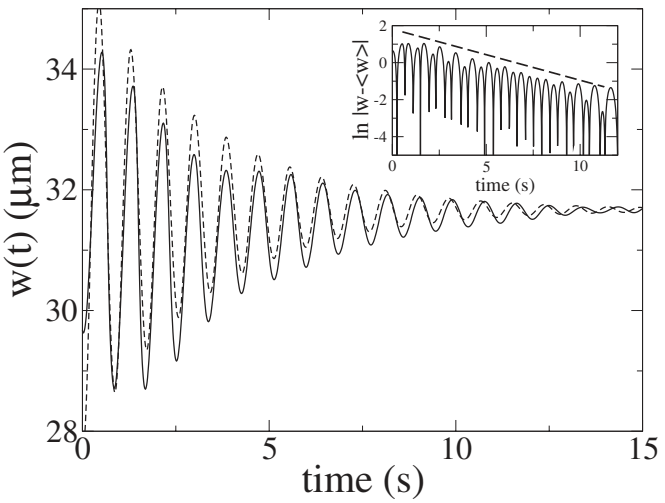

FIG. 8. Decay rate of the noise-induced oscillations after the noise is switched off. The simulations are for $V_p=32$ μm/s, $G=140$ K/cm, $\Lambda=150.2$ μm, and $z'=37.54$ μm. The time evolution can be fitted by (dashed line) $w(t)=w_0e^{\rho t}\cos(\omega t+\omega_0)$, with $\rho=-0.31$ s^{-1} and $\omega=7.38$ rad/s, corresponding to a period of $T=0.85$ s.

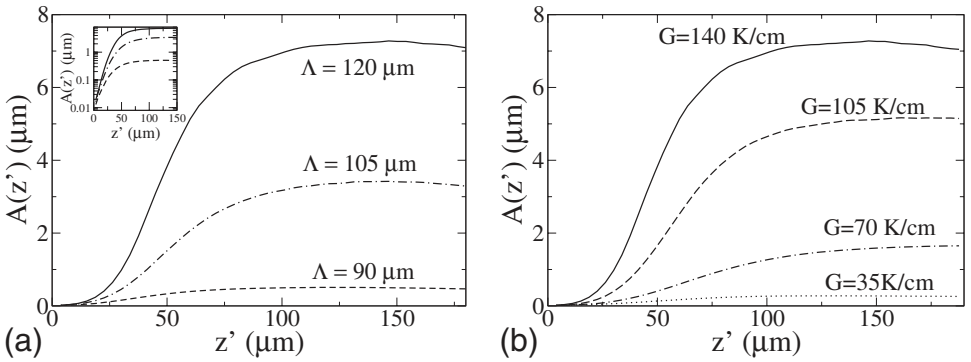

FIG. 9. Amplitude of sidebranching, for $V_p=32\ \mu m/s \simeq 10\ V_c$, as a function of (a) cell spacing for $G=140$ K/cm, and b) thermal gradient, for $\Lambda=120\ \mu m$.

diffusion field at $x=0$ and $x=\Lambda/2$, respectively. In simulations with a full cell we found, however, that the sidebranching amplitude was not significantly different. Consequently, we expect that the present simulations suffice to characterize the essential features of the sidebranching onset in the present context.

For a given gradient, we observe the expected dependence of the onset of sidebranching on velocity and cell spacing. Sidebranching is induced by increasing velocity at fixed primary spacing, or by increasing spacing at fixed velocity. Increasing the pulling speed makes the system more unstable, since then the diffusion length diminishes, and the sidebranches have more room to develop. More relevant here is the fact that for a fixed velocity and wavelength, the present computations produce the same observation as in the experiment of Georgelin and Pocheau [17]. Namely, increasing G increases the amplitude of sidebranching and thus reduces the onset velocity and wavelength of sidebranching. This is illustrated in Fig. 5 where we compare the shapes for three different temperature gradients at fixed velocity and wavelength.

The sidebranching activity was characterized by recording the horizontal displacement of the interface, $w(z',t)=x_{\rm int}(z',t)$, from the central growth axis, where $z'\equiv z_{\rm tip}(t)-z$ is the distance behind the instantaneous tip position. A typical time series is shown in Fig. 6. From the Fourier spectrum it is clear that there is a preferential period that is amplified by the system, with a noisy signal on top of it. It is also apparent the presence of bursts of almost periodic sidebranches of large amplitude. This agrees very well with [17,25], where spatial and temporal coherence of sidebranching was reported. They observed a phase order that extended over five to ten sidebranches, that would correspond to the size of the bursts observed in the present simulations. The period of oscillation changes slightly with G, from $T\simeq 0.88$ s at $G=140$ K/cm ($\lambda_{SB}=V_p/T\simeq 28\ \mu$m) to $T\simeq 0.77$ s at $G=35$ K/cm ($\lambda_{SB}\simeq 25\ \mu$m). The period, however, remains almost constant along the side of the cell.

In Fig. 7, we show the evolution of the tip velocity, and its Fourier spectrum. The first thing to notice is that the fluctuations in the tip velocity are very small, and therefore they cannot be the cause of sidebranching. In order to understand its origin we also plot the Fourier spectrum of the evolution of the interface at several distances behind the tip. It is then clear the emergence of a well-defined frequency as noise is amplified along the interface. This frequency is, however, not present in the Fourier spectrum of the tip velocity. This seems to suggest that there is an intrinsic frequency in the system, a damped oscillatory mode, that is excited by noise. The decay rate can be obtained setting the noise strength to zero, after which sidebranches dissappear (Fig. 8).

From the time series of the position of the interface $w(z,t)$ we calculate the root mean square sidebranching amplitude, defined by

$$A(z')=\sqrt{\langle w(z',t)^2\rangle-\langle w(z',t)\rangle^2}, \tag{29}$$

where $\langle\ \rangle$ denotes a time average. The temporal averages are taken over times of approximately 50 diffusion times $t_D=D/V_p^2$ (ranging from $t_D\sim 1$ s at $V_p=32\ \mu$m/s to $t_D\sim 8$ s at $V_p=8\ \mu$m/s). Plots of $A(z')$ for different gradients and cell spacings are shown in Fig. 9. This figure shows that $A(z')$ has a peak at a distance, z'_{SB}, that decreases when G is increased. As can be seen in Fig. 10, the peak sidebranching amplitude $A_{\rm max}\equiv A(z'_{SB})$ increases exponentially with cell spacing, up to a given spacing, at which sidebranches are constrained by the walls and the amplitude saturates. There is, therefore, no real threshold and the instability

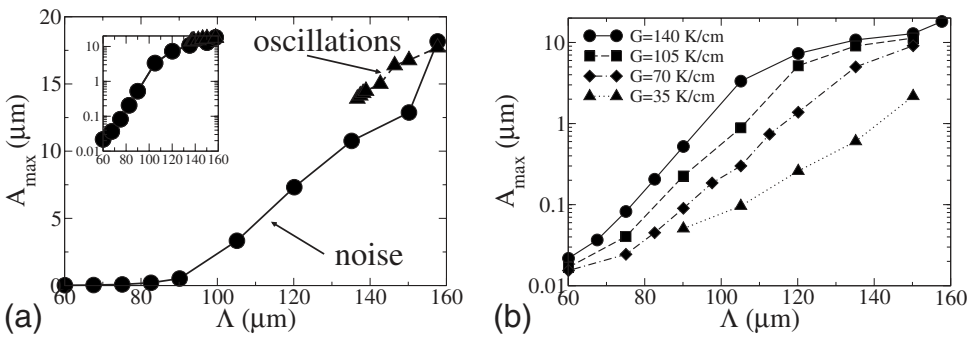

FIG. 10. Maximum amplitude of sidebranching at $V_p=32\ \mu m/s\simeq 10\ V_c$ as a function of cell spacing, (a) for $G=140$ K/cm, and (b) for various values of the thermal gradient.

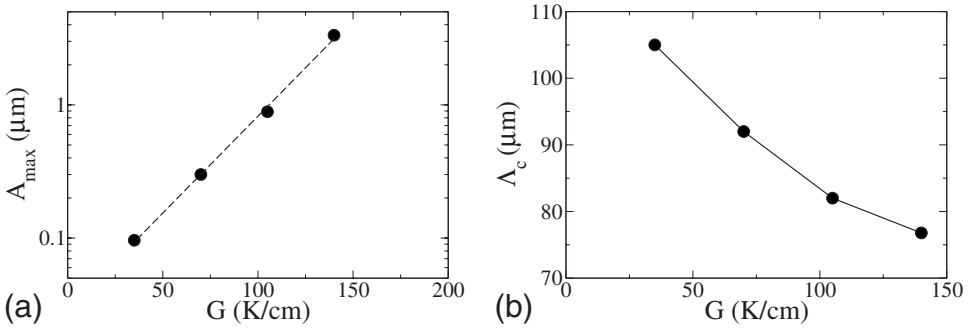

FIG. 11. (a) Maximum amplitude of sidebranching (for $\Lambda = 105\ \mu$m) and (b) critical cell spacing as a function of thermal gradient. The pulling speed is $V_p = 32\ \mu\text{m/s} \simeq 10\ V_c$.

is noise-induced. We define the critical cell spacing for the onset of sidebranching as the value of Λ for which the maximum amplitude $A_{\max} = 0.1\ \mu$m. Clearly this definition is somehow arbitrary, although it roughly corresponds to the experimental accuracy in [17]. As the growth is exponential with the cell spacing, a change in the definition of the critical amplitude would only change slightly the onset. The peak sidebranching amplitude, $A_{\max} \equiv A(z'_{SB})$, increases when G is increased, which gives a quantitative characterization of the thermal gradient enhancement of sidebranching. As can be observed in Fig. 11 the amplitude of sidebranching grows also exponentially with G.

As we have mentioned before, in all these simulations the tip velocity remains almost constant. Thus, the tip motion does not drive sidebranching here, which must be due to noise amplification along the interface. There are two main theories of noise amplification, depending if the amplification is produced on the tip region, or on the sides (see Appendix). Amplification at the tip requires that the wavelength of sidebranching be smaller than the tip radius, and predicts a constant amplification rate. Since none of these agree with the results from the simulations, sidebranching is expected to result from the amplification of noise along the sides. For an isolated cell with arbitrary shape (this is, not taking into account the interaction with the diffusion field of the neighboring cells), the expression for the noise amplification along the sides is

$$A = A_{\text{noise}} \exp[I(z')], \tag{30}$$

$$I(z') = \left\{ \frac{2}{3} \left[\frac{x_0(z';G)^3 V_p \Omega (1 - V_c/\Omega V_p)}{6[k + (1-k)\Omega] d_0 D z'} \right]^{1/2} \right\}. \tag{31}$$

An important consequence of these equations is the prediction that the rate of noise amplification on the sides, and hence the distance from the tip to the first visible sidebranch, is very sensitive to the steady-state shape of the needle crystal. This effect has a simple physical interpretation. The local amplification rate of a perturbation of a fixed wave number q within the wave packet depends on the velocity normal to the interface $V_n = V_p \cos\theta$ [see Eq. (A5)]. It follows that perturbations are amplified at a faster rate if the sides are less steep since $\cos\theta$ is larger.

Therefore, one can see from Eq. (31) that there are two competing effects of the thermal gradient: one destabilizing via the shape, i.e., the fact that $x_0(z';G)^3/z'$ increases with G at fixed z', and the other stabilizing via the thermal gradient. A larger thermal gradient increases the critical pulling speed V_c, and therefore reduces the amplification rate. The amplitude of A_{noise} can be estimated to remain approximately con-

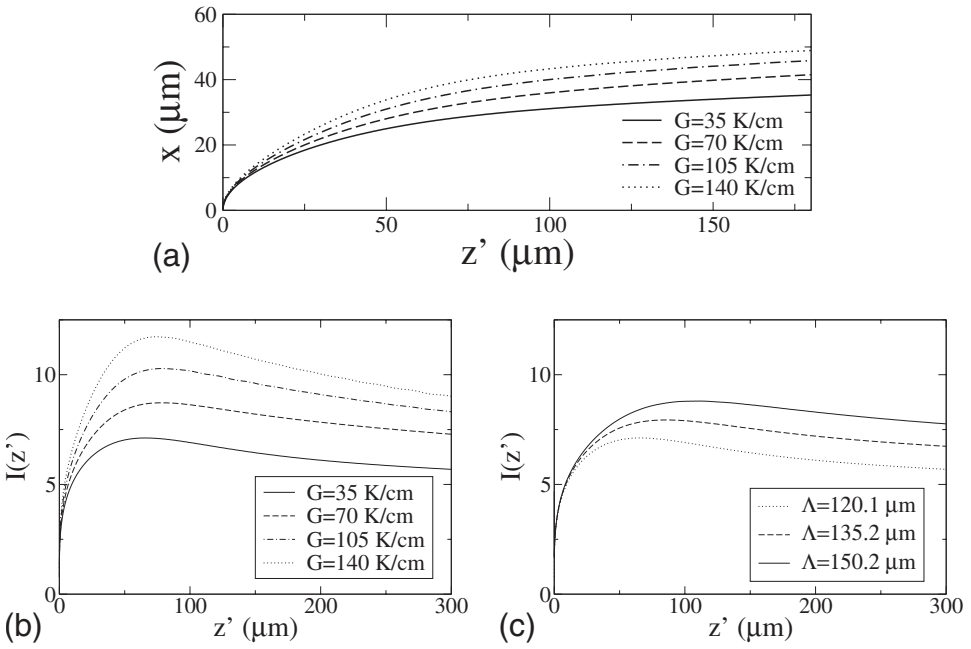

FIG. 12. (a) Steady state shapes obtained simulating the phase-field equations without noise, for four different values of G, and $\Lambda = 120.1\ \mu$m, $V_p = 32\ \mu$m. (b) Amplification rate $I(z')$, as a function of thermal gradient G, for $\Lambda = 120.1\ \mu$m, and $V_p = 32\ \mu$m/s. (c) $I(z')$ as a function of cell spacing for $G = 35$ K/cm.

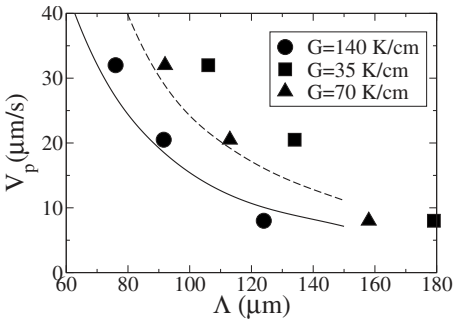

FIG. 13. Onset of sidebranching as a function of cell spacing and pulling speed. The onset is calculated when the maximum amplitude of sidebranching is $A_{max}=0.1$ μm. The lines correspond to a fit of the experimental results in Ref. [17], at $G=140$ K/cm(solid), and $G=36$ K/cm (dashed).

stant for the purpose of interpreting the present simulations because the thermal gradient only damps long wavelength fluctuations of the interface $q \ll (d_0 l_T)^{-1/2}$ that are not selectively amplified. Assuming A_{noise} constant, the effect of G on the sidebranching amplitude is contained solely in the dependence of $I(z';G)$ on G. To compute it, we obtain the cell shapes numerically, simulating the phase-field equations without noise. Figure 12 shows that the main effect of the thermal gradient on the steady-state shape is to render the cell sides less steep behind the tip. This is to be expected since the thermal gradient tends to flatten the interface profile. Evaluating the different terms in Eq. (31), we see that this must be the relevant effect. Undercooling does not change much with thermal gradient, and the dependence of the growth rate with pulling speed is small, since we are always far from onset. In fact, this effect enters Eq. (31) through the term $V_p - V_c \sim V_p$ since in all cases $V_p \gg V_c$. It is, therefore, tempting to conjecture that the thermal gradient enhancement of the sidebranching amplitude is due to this shape change.

In Figs. 12(b) and 12(c), we plot $I(z')$ vs z' with $x_0(z';G)$ taken from the simulated steady-state shapes shown in Fig. 12(a). This plot shows that in fact the effect of the thermal gradient on the shape is enough to explain the enhancement of sidebranching with G. There is also a value of z' at which amplification reaches a maximum, although it happens slightly earlier than in simulations. Furthermore, this maximum is also shifted to larger values of z' as G is increased. After the maximum, the decrease in the amplification rate from Eq. (31) is overestimated. At that point, though, the assumptions under which Eqs. (30) and (31) are obtained are no longer fulfilled, and we should not expect a perfect agreement. From these considerations, one would expect that close to onset, the opposite effect could observed, since then the change in the term $V_p - V_c$ could become relevant, and overcome the effect on the change in cell shape.

In Fig. 13, we compare our phase diagram for the onset of sidebranching with the results obtained in [17]. As expected, only a semiquantitative agreement is obtained. In particular, we find a bigger change in onset as the thermal gradient is changed. This is to be expected, according to the discussion in the previous section. There we found that in our simulations $\rho \sim G$ while in experiments $\rho \sim G^{1/2}$. Thus, the thermal gradient has a bigger effect on cell shapes in our simulations, and that is reflected in a bigger change in onset.

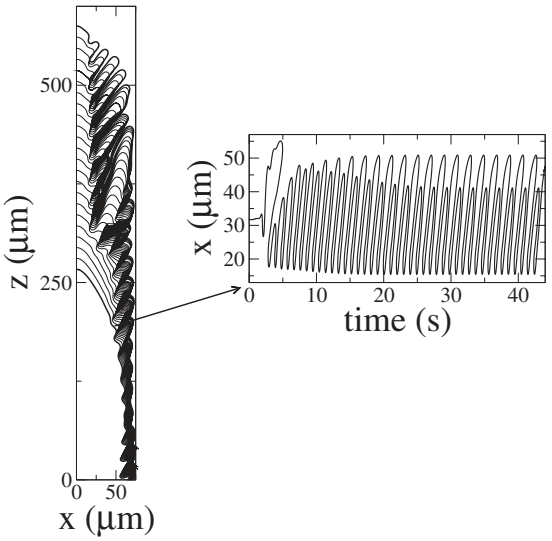

FIG. 14. Evolution of the interface after applying the perturbation in Eq. (32), with $A=0.00016$, $R=1.6$ μm, during a time $t=0.1$ s.

C. Oscillating states

Besides noise amplified sidebranches, we have found that there is also another branch where sidebranches behave deterministically, and are not due to the influence of noise. Such a state can be obtained from a cell state, changing the local temperature at the tip during a time $t \sim \rho / V_p$, with a perturbation

$$U + \frac{z - V_p t}{l_T} \rightarrow U + \frac{z - V_p t}{l_T} + A e^{[(x - x_{tip})^2 + (y - y_{tip})^2]/R^2} \tag{32}$$

in Eq. (18). We choose the width of the Gaussian to be a fraction of the tip radius ($R \sim \rho/5$). If the perturbation is not too strong (in which case the tip splits), the system undergoes a transition to a state with perfectly periodic side-

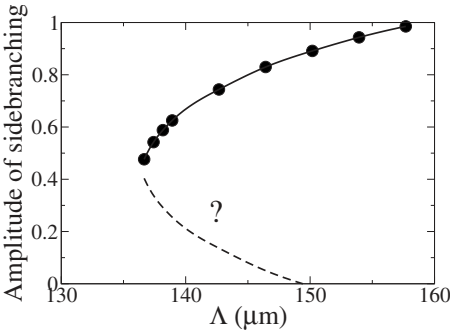

FIG. 15. Amplitude of oscillation, at 3.75 μm behind the tip, as a function of the cell spacing, for $V_p=32$ μm/s, $G=140$ K/cm. The dashed line corresponds to a hypothetical unstable branch.

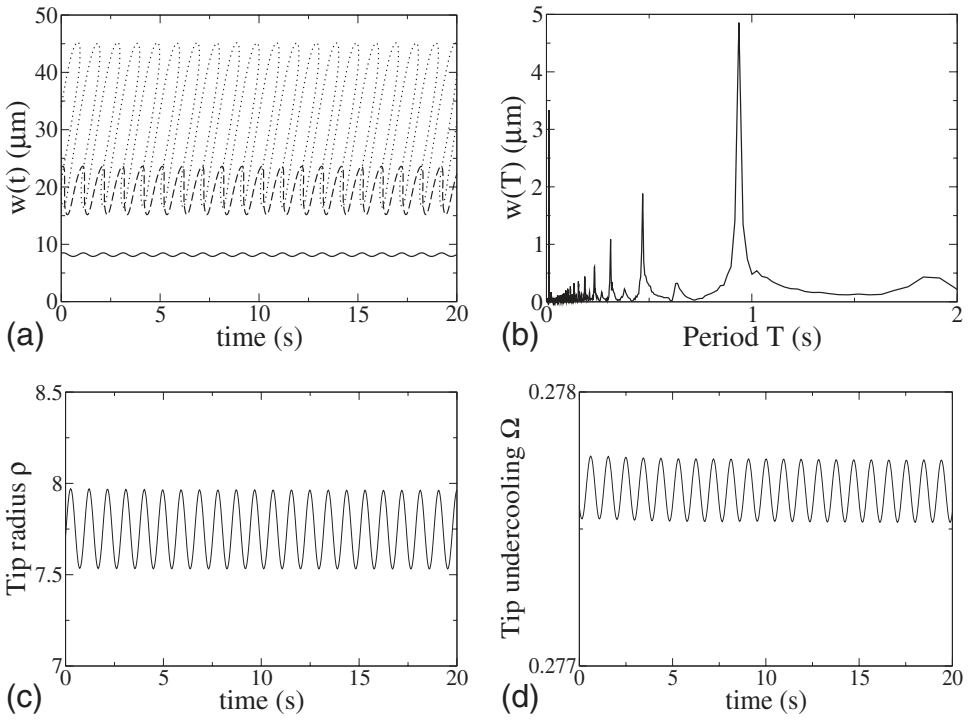

FIG. 16. (a) Amplitude of oscillation, at 3.75 μm (solid), 18.77 μm (dashed), and 37.54 μm (dotted) behind the tip, for $V_p=32$ μm/s, $G=140$ K/cm, $\Lambda=138.9$ μm. (b) Fourier spectrum. The peak is for $T=0.94$ s. (c) Amplitude in tip radius and (d) tip undercooling for the same parameters.

branches (Fig. 14). Studying the amplitude of sidebranching as a function of cell spacing we see that this branch appears through a subcritical Hopf bifurcation from the underlying cell state (Fig. 15), and it persists up to a cell spacing at which tertiary branches develop. This oscillatory state also persists in the presence of noise, in which case there is a noisy response on top of the deterministic oscillations. The bursts of almost perfectly oscillating sidebranches obtained in the previous section (and in experiments, e.g., [25]) are probably due to the presence of a saddle-node remnant, that attracts the orbit for some time, until it goes back to the noisy oscillations close to the cell state.

As can be seen in Fig. 16 the period is very similar, but not exactly the same as for the sidebranches induced by noise. Also the tip position (and curvature) in this case presents oscillations of the same frequency [Fig. 16(c)]. The mechanism of the oscillations is probably due to a feedback between the change in the concentration field at the tip induced by the sidebranches and the amplification of the perturbation along the sides. Note that the frequency here is very different from that obtained in the oscillatory instability at small cell spacings in Sec. IV A. There, there were big oscillations around the tip position that induced periodic changes in the tip radius. Here, the tip position remains almost constant, while the tip radius oscillates. Thus, it seems that sidebranches excite a damped oscillatory mode of the tip. It is also interesting to note that the different dendrites interact in such a way that their corresponding sidebranches oscillate in opposition of phase (Fig. 17).

For other values of the parameters, the hysteretic region can be small, and thermal noise enough to produce a transition to this oscillating state. This is shown in Fig. 18, where the initial condition is a cell without oscillations, at a slightly smaller cell spacing. The sidebranching and tip oscillations grow as the system jumps from the branch corresponding to noise-induced sidebranches to the oscillating cell. For the parameters in Fig. 15, this transition can be achieved increasing the strength of noise, thus assessing the bistability between the cell and oscillating branches.

To make sure that this oscillating state is not an artifact of the two-dimensional nature of our simulations, we have repeated the simulations with three-dimensional cells. As in the experiments, we consider cells in a thin slab of thickness $\delta=36$ μm. We take the parameters $G=140$ K/cm and

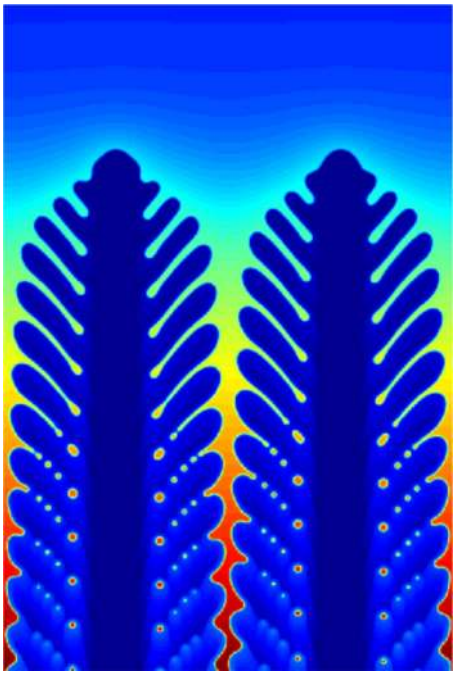

FIG. 17. (Color online) Oscillatory state for $V_p=32$ μm/s, $G=140$ K/cm.

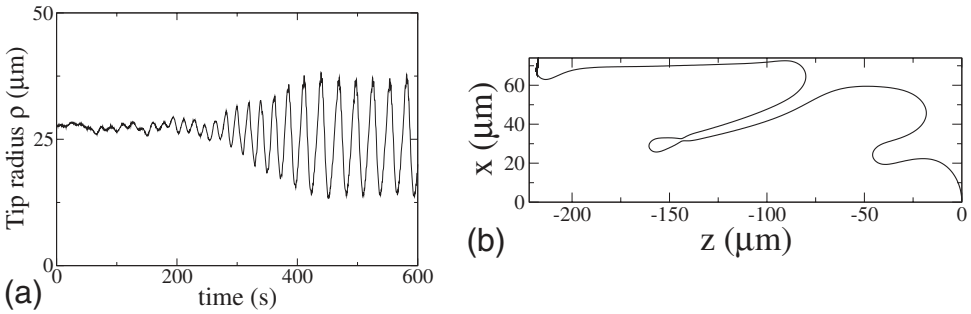

FIG. 18. (a) Tip radius as a function of time and b) final interface profile at $G=140$ K/cm, $V_p=8$ μm/s, and $\Lambda=150.2$ μm.

$V_p=32$ μm/s. The expression for the perturbation is now given by:

$$U_{\text{perturb}} = Ae^{-[(x-x_{\text{tip}})^2+(y-y_{\text{tip}})^2+(z-z_{\text{tip}})^2]/R^2}. \quad (33)$$

The strength of the perturbation has to be set as to avoid tip splitting if too strong, or the relaxation back to the stable state if too weak. Within a range of spacings, this temporary perturbation induces a transition to an oscillatory state, and the resulting shape presents perfectly periodic sidebranches (Fig. 19), while the tip position and curvature oscillate.

As in the bidimensional case, we characterized the oscillatory states by the amplitude of the oscillation at a distance behind the tip. Figure 20 includes a plot showing the evolution of oscillations at several distances behind the tip, as well as the evolution of the tip undercooling (calculated from the tip position) and curvature. The frequency of oscillation of these three quantities is clearly the same, as expected from the feedback mechanism that sustains the oscillations. This is further confirmed by the Fourier spectrum [Fig. 20(d)]. In Fig. 21, we show the oscillation amplitude at a distance of 3.8 μm behind the tip as a function of spacing. This plot suggests that the oscillatory branch appears through a Hopf bifurcation from the stable state, up to a critical spacing beyond which tertiary branches develop, as was found in the bidimensional case. However, in this case, the supercritical or subcritical nature of the bifurcation is not clear. The range for which the oscillatory states exist is shifted toward lower spacings when compared to the bidimensional case, suggesting the role of the additional curvature as a stabilizing factor.

FIG. 19. (Color online) Thin-sample geometry oscillatory state corresponding to $G=140$ K/cm and $V_p=32$ μm for a spacing of $\Lambda=115$ μm and a thickness of $\delta=36$ μm.

V. CONCLUSIONS AND FUTURE PROSPECTS

In summary, we have used a computationally efficient phase-field formulation to investigate the dynamics of sidebranching during directional solidification for realistic parameters of a dilute alloy. Our main finding is that sidebranching can result either from noise amplification or from a nonlinear limit cycle that exists both in two dimensions and in a three-dimensional thin-sample geometry. The oscillatory branch of growth solutions bifurcates subcritically from the main steady-state branch of solutions and exists over a finite range of large array spacings. In contrast, noise-induced sidebranching is associated with a smooth transition where the sidebranching amplitude increases exponentially with spacing up to nonlinear saturation due to the overlap of diffusion fields from neighboring cells.

In the latter case where sidebranching is noise-induced, we have shown that increasing the externally imposed thermal gradient reduces the onset velocity and wavelength of sidebranching, as observed experimentally. We have argued that this counterintuitive effect results from a change in tip shape with increasing thermal gradient, i.e., the cell tip becomes blunter with increasing G, which promotes noise amplification in the tip region. This difference can be attributed to the strong effect of the temperature gradient on the tip dynamics. In particular, this gradient induces a solute gradient along the interface that helps secondary branches grow out of the side regions and rotate toward the growth axis.

Whether sidebranching is caused by noise amplification or a limit cycle has been a long standing issue in solidification for several decades. For freely growing dendrites, theory and experiments support the predominance of a noise amplification scenario. Our results show that the picture is fundamentally different for directional solidification due to the presence of a nonlinear limit cycle, whose existence is demonstrated here for the first time in two and three dimensions. In our simulations in two dimensions, we observe a transition from small noisy sidebranches at small cell spacings, to bursting behavior as we reach the critical spacing for the onset of the limit cycle, and finally, noisy oscillations, when the amplitude of the limit cycle is large. In this picture, the bursting observed in [25] could be explained as coherent

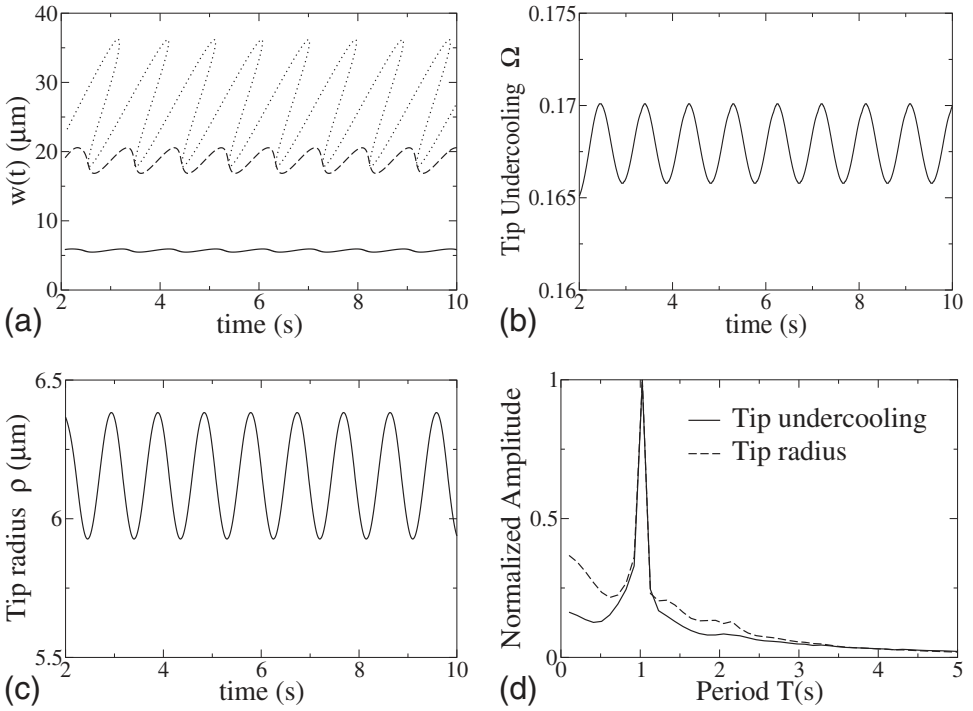

FIG. 20. Time evolution of (a) the oscillations at 3.8 μm (solid), 19 μm (dashed), and 38 μm (dotted line) behind the tip for a spacing of $\Lambda=115$ μm, (b) tip undercooling and (c) tip radius, with (d) the corresponding normalized Fourier spectrum.

oscillations due to noise in a region of parameters below the saddle-node that gives rise to the limit cycle [34]. Additional three-dimensional phase-field simulations that include thermal noise should be able to validate this scenario.

ACKNOWLEDGMENTS

This research was supported by U.S. Department of Energy. B.E. wants to also acknowledge financial support by MCyT (Spain), and by MEC (Spain), under projects Grant Nos. FIS2005-06912-C02-01 and FIS2008-06335-C02-01. We thank Marc Georgelin and Alain Pocheau for valuable exchanges.

APPENDIX: THEORIES OF NOISE AMPLIFICATION

In this section, we interpret our results within the existing theories of noise amplification. We find that none of the existing analyses reproduces quantitatively our simulation results, whether based on noise amplification at the tip or on the sides of freely growing needle crystals. This is to be expected, at least for the latter case, since noise amplification is strongly affected by the interaction of the diffusion fields between neighboring cells. Nonetheless, the examination of these limits allows us to better pinpoint the factors that govern the onset of sidebranching and the role of the thermal gradient.

1. Noise amplification at the tip

One idea, developed originally by Zel'dovich in the context of flame fronts [35], consists of calculating the amplification rate of a normal localized perturbation of amplitude, $A_{\text{noise}}/\rho \ll 1$, as it is advected along the interface at a tangential speed $V \sin\theta$. One can assume this perturbation to be localized at a distance from the tip comparable to the stability length, λ_s, at which the amplification rate $\omega(\lambda)$ of sinusoidal perturbations of wavelength λ of the planar interface vanishes. As this perturbation is advected away from the tip, its wavelength λ is stretched and hence it becomes amplified since $\omega(\lambda)>0$ for $\lambda>\lambda_s$. The amplitude A at a given arclength distance s along the interface from the tip can then be calculated by a WKB approximation, which assumes that $\lambda_s/\rho \ll 1$. This analysis yields an exponential amplification,

$$A = A_{\text{noise}} \exp(I_{\text{tip}}), \quad (\lambda_s \ll s \ll \rho), \tag{A1}$$

where

$$I_{\text{tip}} = \frac{4\pi\rho}{3\lambda_s} = \frac{2\rho}{3\sqrt{l_D d_0/\chi}} \sqrt{2/(1+D_s/D_l) - \chi l_D/l_T}. \tag{A2}$$

It is important to emphasize that A is independent of s because the dominant part of the amplification occurs in the region closest to the tip where the advection speed is the smallest. The first equality above applies to an arbitrary

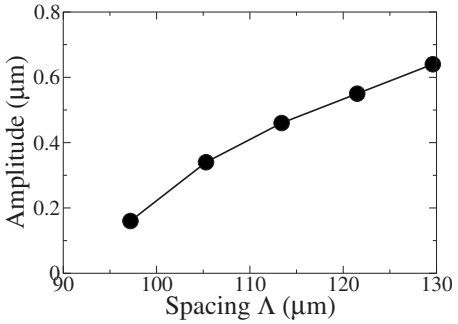

FIG. 21. Amplitude of oscillation at a distance of 3.8 μm behind the tip as a function of cell spacing.

curved front (flame, viscous finger, etc.) where the noise amplification is dominated by the tip region, and the second equality applies specifically to directional solidification. It is obtained by substituting the expression for λ_s at the cell tip where D_s and D_l are the solute diffusivities in the solid and liquid, respectively, and $\chi=\Delta c_{\text{tip}}/\Delta c_0=c_l/c_l^0$ is the ratio of the concentration jump across the solid-liquid interface evaluated at the tip temperature, and at the reference temperature of the steady-state planar interface. This equation was written down by Sarkar for the case where $D_s=0$ [36] and is written down here for an arbitrary diffusivity ratio.

The effect of the thermal gradient is subtle because I_{tip} has both: (i) an explicit dependence on G via $l_T \sim G^{-1}$, and (ii) an implicit dependence on G via ρ and χ. The first is readily seen to be stabilizing (i.e., increasing G decreases I_{tip}), contrary to experiment, whereas the second may be either stabilizing or destabilizing depending on the dependence of the tip radius and temperature on the thermal gradient. In our simulations $\rho, \Omega \propto G$, so they provide a destabilizing effect. In fact, I_{tip} increases with thermal gradient G. Hence, it is not *a priori* incompatible with the observations in the simulations. However, this theory *assumes* that noise amplification occurs predominantly in the tip region. While this assumption is justified for other interfacial pattern forming systems (flame fronts, viscous fingers in a Hele Shaw geometry, etc.) where the growth of perturbations normal to the interface is suppressed by the walls in the region behind the tip, it remains unclear whether it is justified for solidification cells. Pocheau and Gorgelin, for example, have concluded that Eq. (A2) does not seem to predict the correct G-dependence of the sidebranching onset in their experiments. Figure 9 clearly shows that the sidebranching amplitude reaches a maximum at distance of several tip radii behind the tip. This result is therefore incompatible with the assumption, on which Eq. (A2) is based, that noise amplification occurs predominantly in the tip region. The condition of validity of the WKB analysis ($\lambda_s \ll \rho$) leading to Eq. (A2) is also violated. Thus, this theory does not describe correctly the amplification of noise in our simulations. Near the onset of sidebranching, cell shapes are somewhat intermediate between viscous fingers and free dendrites where amplification is dominated by the sides.

2. Noise amplification on the sides

The WKB analysis of Zel'dovich was extended to dendritic growth by Pelcé [37], and Pelcé and Clavin [38]. They made the important observation that noise amplification along the sides of free dendrites is dominated by the region far behind the tip ($z' \gg \rho$). In this case, the WKB analysis leads to the result that A reaches a maximum value at a distance from the tip that is fixed by the initial wavelength λ (or frequency $\omega=2\pi V/\lambda$) of the perturbation. Since, for any given wavelength, this perturbation eventually dies out far from the tip, a finite threshold amplitude of noise is necessary to produce a finite (visible) sidebranching amplitude. Subsequently, Pieters and Langer using a boundary layer model [5], and then Barber *et al.* [6] in a nonlocal model, correctly argued that a wave packet localized initially near the tip contains an infinite range of frequencies. Therefore, this wavepacket will continue to grow indefinitely far from the tip because arbitrarily low frequencies are amplified arbitrarily far from the tip. In this picture, there is no threshold of sidebranching that can occur arbitrarily far from the tip for an arbitrarily small noise. The sidebranching amplitude at a distance z' behind the tip is given by the relation, valid in two or three dimensions for $z' \gg \rho$

$$A(z') = A_{\text{noise}} \exp[I(z')], \tag{A3}$$

$$I(z') = \frac{2}{3}\left[\frac{V x_0(z')^3}{6 D d_0 z'}\right]^{1/2}. \tag{A4}$$

An expression for A_{noise} was derived by Langer in three dimensions together with an expression for $I(z')$ that is equivalent to Eq. (A4) above, but restricted to a paraboloid of revolution (parabola in two dimensions), with $x_0(z')=\sqrt{2\rho z'}$. The expression above for an arbitrary steady-state profile $x_0(z')$ was subsequently derived by Brener and Temkin [8]. A simple alternate derivation is also given in a phase-field modeling study of noise-induced sidebranching in pure melts [9].

To investigate this further, let us extend the prediction of Eq. (A4) to directional solidification. This extension is only legitimate, of course, in the limit $\Lambda \gg l_D$ where the overlap of the diffusion fields between dendrites can be neglected in the region behind the tip up to the first visible sidebranch ($A/\Lambda \sim 1$). Clearly, far enough behind the tip the diffusion fields must eventually overlap since the liquid fraction goes to zero. Therefore, this extension will only be valid over some intermediate region between the tip and the narrow grooves. When a thermal gradient is included, the local amplification rate of a perturbation of fixed wave number q, on an interface at position $z_{\text{tip}}=(1-\Omega)/l_T$, is

$$\omega(q) = \{V_n \Omega q(1 - l_D/2\Omega l_T) - 2 D d_0 q^3\}/[k + (1-k)\Omega], \tag{A5}$$

where $V_n=V_p \cos\theta$ is the pulling speed in the direction normal to the interface, the extra factor $(1-l_D/2\Omega l_T)$ that multiplies V_n reflects the "stabilizing" effect of the thermal gradient, and the term $k+(1-k)\Omega$ appears because of the dependence of the local surface tension on the tip position. Repeating the wave packet analysis leading to Eq. (A4), using Eq. (A5), leads to the result

$$A(z';G) = A_{\text{noise}} \exp[I(z';G)], \tag{A6}$$

$$I(z';G) = \frac{2}{3}\left[\frac{V_p \Omega(1 - l_D/2\Omega l_T) x_0(z';G)^3}{6[k + (1-k)\Omega] D d_0 z'}\right]^{1/2}. \tag{A7}$$

Some analytical theory seems needed to better understand and characterize the interaction of a growing perturbation on the cell sides with a wall. So far, however, we have not found a simple way to proceed to develop such a theory, except in limiting cases that do not pertain directly to our simulations or experiments.

[1] W. Kurz and D. J. Fisher, *Fundamentals of Solidification* (Trans Tech, Switzerland, 1989).
[2] S.-C. Huang and M. E. Glicksman, Acta Metall. **29**, 701 (1981); **29**, 717 (1981).
[3] U. Bisang and J. H. Bilgram, Phys. Rev. Lett. **75**, 3898 (1995).
[4] J. C. LaCombe, M. B. Koss, V. E. Fradkov, and M. E. Glicksman, Phys. Rev. E **52**, 2778 (1995).
[5] R. Pieters and J. S. Langer, Phys. Rev. Lett. **56**, 1948 (1986).
[6] M. N. Barber, A. Barbieri, and J. S. Langer, Phys. Rev. A **36**, 3340 (1987).
[7] J. S. Langer, Phys. Rev. A **36**, 3350 (1987).
[8] E. Brener and D. Temkin, Phys. Rev. E **51**, 351 (1995).
[9] A. Karma and W.-J. Rappel, Phys. Rev. E **60**, 3614 (1999).
[10] J. S. Langer, Rev. Mod. Phys. **52**, 1 (1980).
[11] W. W. Mullins and R. F. Sekerka, J. Appl. Phys. **34**, 323 (1963); **35**, 444 (1964).
[12] V. Seetharaman and R. Trivedi, Metall. Trans. A **19**, 295 (1988); M. A. Eshelman, V. Seetharaman, and R. Trivedi, Acta Metall. **36**, 1165 (1988); V. Seetharaman, M. A. Eshelman, and R. Trivedi, *ibid.* **36**, 1175 (1988).
[13] P. Kurowski, C. Guthmann, and S. de Cheveigné, Phys. Rev. A **42**, 7368 (1990).
[14] R. Trivedi, Y. Shen, and S. Liu, Metall. Mater. Trans. A **34**, 395 (2003).
[15] J. D. Hunt and S.-Z. Lu, Metall. Mater. Trans. A **27**, 611 (1996).
[16] S. Gurevich, A. Karma, M. Plapp, and R. Trivedi, Phys. Rev. E **81**, 011603 (2010).
[17] M. Georgelin and A. Pocheau, Phys. Rev. E **57**, 3189 (1998).
[18] A. Pocheau and M. Georgelin, Eur. Phys. J. B **21**, 229 (2001).
[19] A. Pocheau and M. Georgelin, J. Cryst. Growth **250**, 100 (2003).
[20] M. Georgelin, S. Bodea, and A. Pocheau, EPL **77**, 46001 (2007).
[21] G. P. Ivantsov, Dokl. Akad. Nauk SSSR **58**, 567 (1947).
[22] M. Mashaal, M. Ben Amar, and V. Hakim, Phys. Rev. A **41**, 4421 (1990).
[23] O. Martin and N. Goldenfeld, Phys. Rev. A **35**, 1382 (1987).
[24] D. A. Kessler and H. Levine, Phys. Rev. Lett. **57**, 3069 (1986).
[25] A. Pocheau, S. Bodea, and M. Georgelin, Phys. Rev. E **80**, 031601 (2009).
[26] A. Karma, Phys. Rev. Lett. **87**, 115701 (2001).
[27] B. Echebarria, R. Folch, A. Karma, and M. Plapp, Phys. Rev. E **70**, 061604 (2004).
[28] A. Karma, Phys. Rev. E **48**, 3441 (1993).
[29] A. Karma and W. J. Rappel, Phys. Rev. E **53**, R3017 (1996); Phys. Rev. Lett. **77**, 4050 (1996); Phys. Rev. E **57**, 4323 (1998).
[30] R. Trivedi, S. Liu, B. Echebarria, and A. Karma, in *Solidification Processes and Microstructures* (The Minerals, Metals, and Materials Society, Warrendale, PA, 2004), pp. 307–318.
[31] M. Georgelin and A. Pocheau, J. Cryst. Growth **268**, 272 (2004).
[32] A. Pocheau and M. Georgelin, J. Cryst. Growth **206**, 215 (1999).
[33] A. Karma and P. Pelce, Phys. Rev. A **39**, 4162 (1989).
[34] Hu Gang, T. Ditzinger, C. Z. Ning, and H. Haken, Phys. Rev. Lett. **71**, 807 (1993).
[35] Ya. B. Zel'dovich, A. G. Istratov, N. I. Kidin, and V. B. Librovich, Combust. Sci. Technol. **24**, 1 (1980).
[36] S. K. Sarkar, Phys. Lett. A **117**, 137 (1986).
[37] P. Pelce, Ph.D. Thesis, Université de Provence (1986).
[38] P. Pelce and P. Clavin, EPL **3**, 907 (1987).